www.sciencemag.org/content/360/6386/296/suppl/DC1

Supplementary Materials for

Capillarity-induced folds fuel extreme shape changes in thin wicked membranes

Paul Grandgeorge, Natacha Krins, Aurélie Hourlier-Fargette, Christel Laberty-Robert, Sébastien Neukirch, Arnaud Antkowiak*

*Corresponding author. Email: arnaud.antkowiak@upmc.fr

Published 20 April 2018, *Science* **360**, 296 (2018)
DOI: 10.1126/science.aaq0677

This PDF file includes:

Other supplementary material for this manuscript includes the following:

Materials and Methods

Materials

The polymers used to fabricate the fibrous membranes are Poly(vinylidene fluoride-co-hexafluoropropylene) (PVDF-HFP, Solvay), Polyacrylonitrile (PAN, M.W. 150,000, Sigma Aldrich), Polycaprolactone (PCL, M.W. 80,000, Sigma Aldrich) and Polyvinylpyrrolidone (PVP, M.W. 1,300,000, Acros Organic). The solvents are n,n-dimethylformamide (DMF, Carlo Erba Reagents) and ethanol (absolute, Sigma Aldrich). The concentration of polymer of each polymer/solvent solution is 10% weight. The liquids used to wick the fibrous membranes are deionized water, glycerol (Sigma Aldrich), ethanol (absolute, Sigma Aldrich) and silicone oils (Sigma Aldrich). A summary of the constituents is provided in Table S1. Surface tensions of liquids are characterized using a Krüss K6 manual tensiometer (hanging ring). Erioglaucine disodium salt (Sigma Aldrich) is used to dye the fibrous membrane (dissolution of the coloring agent in the polymer/solvent solution prior to electrospinning) and deionized water for colorimetry purposes. 1 mm-wide gold strips are obtained by manually cutting 100 nm-thick edible gold leaves (purchased from Alice Delice) using a surgical blade.

Fibrous membrane preparation

The fibrous membranes are obtained using an electrospinning apparatus ES-1A (Electrospinz Ltd.) following these steps:

1. A polymer is dissolved in a solvent (the polymers and corresponding solvents that are used in this work are presented in Table S1).

2. The solution is injected through an electrically charged blunt needle (diameter of the needle: 1 mm, injection rate: 0.02 ml/min, applied voltage: between 10 and 15 kV). The outgoing droplet is destabilized through the formation of a Taylor cone which is ejected as a liquid rod towards an electrically earthed plane target (distance between the tip of the needle and the target: 17cm). As it travels towards the target, the solvent evaporates from the liquid rod which therefore quickly undergoes a swirling instability which randomly deviates it.

3. The resulting fibrous mat (made of the addition of solid fibers continuously spun) is recovered from the target, which was previously covered with anti-adhesive cooking paper (purchased from Monoprix S.A.) to avoid sticking.

Once the membrane is attached to the mobile supports (Thorlabs translational elements or laser cut PMMA assembly of eight translational supports), it is wicked by a wetting liquid (see Table S1) using a Terumo 10-ml syringe or a spray. Upon compression, the surface reservoirs are formed through the wrinkling and folding of the membrane under the capillary forces.

Thickness characterization of the wicking liquid film

For the study the wrinkling wavelength λ as a function of the liquid thickness h, a colorimetry tool is used to characterize the liquid film thickness. The membrane is wicked by a dyed liquid (water, dyed blue) and a photograph of the wicked membrane is taken next to a calibration wedge containing the same dyed liquid with a D810 Nikon camera. Comparing the photograph's local gray value on the membrane and the thickness versus the gray value curve (see figure S1), we locally estimate the thickness of the liquid film. Image analysis is performed using the image processing package ImageJ (distribution: Fiji).

Wavelength measurement

The wrinkling wavelength λ is measured when the wicked membrane is slightly compressed. The membrane is illuminated from the side in order to enhance the wrinkles' contrast and a photograph is taken with a D810 Nikon Camera. For each liquid film thickness (different amount of wicked liquid), a set of four wavelength measurements is performed. The coloring agent (erioglaucine disodium salt) does not change the water surface tension significantly. A typical photograph allowing the wavelength measurement is presented in figure S2.

Force measurement and fatigue characterization

The force-versus-displacement curve of the planar wicked membrane is performed using a cantilever beam method on a silicone oil-wicked PVDF-HFP fibrous membrane. The cantilever beam's mechanical response was calibrated using weights (weighed with a Mettler-Toledo MS 0.01 mg precision scale). The membrane is supported by two floating rafts on a water bath to ensure frictionless translational supports. The presented extension/compression force measurement cycles are performed at around 1 mm/s but show little sensitivity to displacement velocity (the same force-versus-displacement curve was obtained for a twice-as-fast displacement speed).
The fatigue test was performed on a silicone oil wicked PVDF-HFP fibrous membrane mounted on a crank rod system (presented in Figure S3) and the wicked membrane underwent 3 extension-compression cycles per second. The compression/extension cycle corresponds to an end to end distance X varying from $X_{\min} = 2$ mm to $X_{\max} = 3.7$ cm. The membrane was re-wicked with silicone-oil every 20,000 cycles to avoid drying. Small circular holes (hundreds of microns in diameter) appeared at around 60,000 cycles, slowly growing up to 150,000 cycles. At this last point, the holes had a significant impact on the mechanical behavior of the wicked membrane (see fig S4) and the membrane tore off shortly after.

Catenoid neck radius measurement

To study the equilibrium forms adopted by a wicked membrane in a cylindrical configuration, a PAN membrane is attached on the edge of two laser cut PMMA rings (diameter $2R = 4$ cm) with 3M double face tape. The membrane is wicked with deionized water and the distance between the two rings is controlled using a Thorlabs 25 mm manual translation stage. Throughout the compression/extension cycle, the shape adopted by the wicked membrane is filmed with a Nikon D810 camera and image post-processing (Python version 2.7.10) allows to measure the neck radii of the resulting catenoid for the visited ring distances. Figure S5 shows a sequence of such compression/extension cycle and makes it clear that the shape adjustments of the wicked membrane are mediated by folds within the liquid film that act as surface reservoirs.

Wicked membrane bubble pressure measurement

To measure the pressure inside an inflated spherical wicked membrane (PAN fibrous membrane wicked with deionized water), visualization of an adjacent ethanol filled tube is used. The bubble is inflated with air using a PHD Ultra Syringe Pumps (Harvard apparatus) at a rate of 6 ml/min. The air-entrance tube is connected to a U-shaped tube partially filled with dyed ethanol with a T-junction. One end of the U-shaped tube is therefore pneumatically linked to the bubble, while the other end is open (at atmospheric pressure). The difference in height Δh of the two ethanol interfaces inside the U-shaped tube indicates the pressure P inside the bubble, knowing its density $\rho = 789$ kg/m^3 and earth acceleration $g = 9.81$ m/s^2 ($P = \rho g \Delta h$). The pressure P is normalized by $P_{\max} = 4\gamma/R_{\text{tube}}$, which is the theoretical maximum pressure for a spherical bubble of surface tension γ, inflated out of cylindrical tube of radius R_{tube} ($R_{\text{tube}} = 4.5$ mm in our experiment). It is to be mentioned that in contact with the PAN membrane, the surface tension of deionized water drops from 72 to 53 mN/m.

Design of a basic stretchable electronic circuit on a wicked membrane

The resistance of the 1 mm-wide, 100 nm-thick gold strip was characterized directly on a silicone oil-wicked PVDF-HFP membrane for different compression states of the membrane. The setup and the resistance-measurements are presented in Figure S7. End-to-end resistance of this path shows to slightly depend on the compression state of the membrane as it decreases when the straight edges of the membrane are brought closer. This behavior is probably due to self-contact of the gold strip when it folds within the membrane reservoirs, thus shortening the effective length of the gold strip, leading to a resistance drop.

Wrinkling wavelength theory

Here, we study the buckling of an elastic beam of total length L confined inside a liquid film of thickness h. The potential energy of the system comprises two terms: the deformation energy of the beam and the surface energy of the liquid/air interface. We impose an end-shortening ΔL on the end-to-end distance of the system. The beam tries to accommodate this imposed constraint by developing a shape with a long axial wavelength, the end-shortening generating a transverse deflection of the beam. This deflection then induces an important deformation of the liquid/air interface and hence raises the surface energy of the interface. A trade-off has to be found between elastic and surface energies, where the total potential energy is minimum.

The present analysis is one dimensional and the energies presented here are considered per unit of depth (in the z direction). As the thickness of the liquid film h is very small compared to the total contour length L of the beam, boundary conditions at the ends of the beam are not considered. The elastic deformation energy of the beam is written as

$$E_{\mathrm{e}} = \frac{1}{2} B \int_0^{L-\Delta L} \kappa^2(x)\, dx \quad \text{with} \quad \kappa(x) = \frac{y''(x)}{[1+y'^2(x)]^{3/2}} \tag{1}$$

where B is the bending stiffness of the beam, $y(x)$ is the elastic beam shape, and $\kappa(x)$ is the curvature of the beam, see figure S8. The surface energy of the liquid/air interface is given by

$$E_\gamma = 2\gamma \int_0^{L-\Delta L} \sqrt{1+{y_\gamma}'^2(x)}\, dx \tag{2}$$

where $y_\gamma(x)$ represents the lower liquid/air interface. The factor 2 in Eq. (2) arises from the top/down symmetry, the upper and lower interfaces having the same lengths. The total energy $E_{\mathrm{e}}+E_\gamma$ of the system has to be minimized under the two following constraints. First the total liquid volume V is conserved. Per unit depth we have $V = hL$, with

$$2\int_0^{L-\Delta L} \big[y(x) - y_\gamma(x)\big]\ dx = V \tag{3}$$

where we only consider the liquid confined between the lower interface and the beam, the factor 2 accounting for the upper half of the liquid. Second, as the beam is considered inextensible, its total contour-length remains unchanged in the deformed configuration:

$$\int_0^{L-\Delta L} \sqrt{1+y'^2(x)}\, dx = L \tag{4}$$

Finally the beam has to stay between the upper and lower liquid/air interfaces. As the upper and lower interfaces are symmetric, we focus on the lower interface $y_\gamma(x)$ and write the inequality constraint

$$y(x) \geq y_\gamma(x) \quad \text{for all } x \in (0; L-\Delta L) \tag{5}$$

The periodic wave ansatz

The present problem resembles a buckling-on-elastic-foundation problem. In such problems the buckling shape is x-periodic. Here the 'foundation' is the liquid/air interface and we conjecture that the shapes of the beam and of the interface are periodic also; we call λ is period. The integrals in Eqs. (1)-(4) are then rewritten as

$$\int_0^{L-\Delta L} \cdots \, dx = N \int_0^{\lambda} \cdots \, dx \tag{6}$$

where the number of waves is $N = (L - \Delta L)/\lambda$. We therefore focus on one wave length and position the origin in x at a maximum in $y(x)$, see Fig. S9.

Non-dimensionalization

Using $L_{\rm ec} = \sqrt{B/\gamma}$ as unit length and $B/L_{\rm ec}$ as unit energy, we introduce the following dimensionless quantities:

$$x_{\rm new} = \frac{x_{\rm old}}{L_{\rm ec}} \; ; \quad y_{\rm new} = \frac{y_{\rm old}}{L_{\rm ec}} \; ; \quad y_{\gamma_{\rm new}} = \frac{y_{\gamma_{\rm old}}}{L_{\rm ec}} \; ; \quad L_{\rm new} = \frac{L_{\rm old}}{L_{\rm ec}} \; ; \quad \lambda_{\rm new} = \frac{\lambda_{\rm old}}{L_{\rm ec}} \; ; \tag{7a}$$

$$h_{\rm new} = \frac{h_{\rm old}}{L_{\rm ec}} \; ; \quad \kappa_{\rm new} = \kappa_{\rm old} L_{\rm ec} \; ; \quad E_{e{\rm new}} = \frac{E_{e{\rm old}} L_{\rm ec}}{B} \; ; \quad E_{\gamma_{\rm new}} = \frac{E_{\gamma_{\rm old}} L_{\rm ec}}{B} \; ; \tag{7b}$$

and work from now on with the new variables without using the 'new' subscript.

Interface $y_\gamma(x)$

We focus on the lower liquid/air interface. As in shown figure S9, along one wave-length $x \in (-\lambda/2; \lambda/2)$ the interface and the beam merge for $|x| > x_\gamma$ and are separated otherwise. The inequality constraint (5) is then replaced by

$$y(x) \;\; = \;\; y_\gamma(x) \text{ for } |x| \geq x_\gamma \tag{8}$$

$$y(x) \;\; > \;\; y_\gamma(x) \text{ for } |x| < x_\gamma \tag{9}$$

The liquid is therefore confined in $|x| < x_\gamma$ and volume conservation (3) reads

$$h - 2\frac{1-\Delta}{\lambda} \int_{-x_\gamma}^{x_\gamma} \big[y(x) - y_\gamma(x) \big] \, dx = 0 \tag{10}$$

As h is small compared to the gravito-capillary length $\sqrt{\gamma/(\rho g)}$, the pressure is nearly uniform inside the liquid film. The interface $y_\gamma(x)$ is then a circular arc of radius R and center $(0; y_c)$, yielding the implicit equation $x^2 + (y_\gamma - y_c)^2 = R^2$. The two unknowns R and y_c are found with the following two conditions. First, the arc touches the beam at $x = \pm x_\gamma$

$$y_\gamma(x_\gamma) = y(x_\gamma) \tag{11}$$

Second, as the liquid wets the beam perfectly, the beam and interface tangents have to coincide at $x = \pm x_\gamma$

$$y'_\gamma(x_\gamma) = y'(x_\gamma) \tag{12}$$

These two conditions are used to express R and y_c as

$$y_{\rm c} = y(x_\gamma) + \frac{x_\gamma}{y'(x_\gamma)} \quad \text{and} \quad R = x_\gamma \sqrt{1 + \frac{1}{y'^2(x_\gamma)}} \tag{13}$$

and we finally write the liquid/air interface equation as

$$y_\gamma(x) = \sqrt{x_\gamma^2 + \frac{x_\gamma^2}{y'^2(x_\gamma)} - x^2} + y(x_\gamma) + \frac{x_\gamma}{y'(x_\gamma)} \tag{14}$$

Summary

In conclusion, the minimization of the potential energy under the constraints of conserved volume and conserved contour length is treated by introducing the Lagrangian

$$\begin{aligned} \mathcal{L} &= \mathcal{L}(y(x), y'(s), y_\gamma(x), y'_\gamma(x), \lambda, x_\gamma) \\ &= \frac{1-\Delta}{\lambda} \int_0^{\lambda/2} \kappa^2(x)\, dx + 4\frac{1-\Delta}{\lambda} \int_0^{x_\gamma} \sqrt{1 + y'^2_\gamma(x)}\, dx + 4\frac{1-\Delta}{\lambda} \int_{x_\gamma}^{\lambda/2} \sqrt{1 + y'^2(x)}\, dx + \\ &\quad \mu_1 \left(h - 4\frac{1-\Delta}{\lambda} \int_0^{x_\gamma} \left[y(x) - y_\gamma(x) \right] dx \right) - \mu_2 \left(1 - 2\frac{1-\Delta}{\lambda} \int_0^{\lambda/2} \sqrt{1 + y'^2(x)}\, dx \right) \end{aligned} \tag{15}$$

where we have used $N = (L - \Delta L)/\lambda$ and divided by the constant L. We also have used the $x \to -x$ symmetry and focused on the positive x part of the system. Equilibrium of the system is found by considering the conditions for which the first variation of this Lagrangian vanishes. The Lagrange multiplier μ_1 associated with volume constraint is interpreted as the pressure inside the liquid (per unit depth, per unit length). The Lagrange multiplier μ_2 associated with inextensibility constraint is related to the tension inside the beam.

Energy minimization for a sinusoidal buckling pattern

In order to simplify the problem, we restrict ourselves to sinusoidal buckling patterns of wavelength λ for the elastic beam, *i.e.* $y(x) = A\cos\left(\frac{2\pi}{\lambda}x\right)$. The liquid/air interface (14) then writes

$$y_\gamma(x) = \sqrt{x_\gamma^2 + \left(\frac{\lambda x_\gamma}{2\pi A \sin\left(\frac{2\pi}{\lambda} x_\gamma\right)} \right)^2 - x^2} + A\cos\left(\frac{2\pi}{\lambda} x_\gamma\right) - \frac{\lambda x_\gamma}{2\pi A \sin\left(\frac{2\pi}{\lambda} x_\gamma\right)} \tag{16}$$

and the Lagrangian (15) is now a simple function $\mathcal{L} = \mathcal{L}(A, \lambda, x_\gamma)$. Minimization is performed numerically and results are presented in figure (S10).

Considering a non-zero thickness of a porous beam

Experimentally, the wrinkling wicked membrane has a non-zero thickness. In the model, the thickness of the beam is taken into account by considering a vertical shift of the liquid interface. The vertical position (13) of the center of the circular arc described by the liquid/air interface is then shifted and we now have

$$y_c = A\cos\left(kx_\gamma\right) - \frac{x_\gamma}{Ak\sin(kx_\gamma)} - \frac{t}{2} \tag{17}$$

where t is the thickness of the beam. Additionally the membrane is porous and entirely wicked by the liquid. Volume conservation is then rewritten as

$$h - t = 4\frac{1-\Delta}{\lambda}\int_0^{x_\gamma}\left[y(x) - \frac{t}{2} - y_\gamma(x)\right]\,dx \tag{18}$$

Please note that (17) and (18) are only valid for small deflections $|y'(x)| \ll 1$, *i.e.* small end-shortening Δ. In this study, we consider the membrane to grow as the liquid film gets thicker, i.e. the membrane thickness t is proportional to the liquid film thickness h wicking it (we use $t = 0.8h$). However, we do not consider the bending stiffness per unit depth B to change during this growth.

Graphical results and discussion

Figure S10 presents the dimensionless wavelength λ versus the dimensionless liquid thickness h for PAN fibrous membranes of different thicknesses wicked by different liquids. Both λ and h are normlized by the elastocapillary length $L_{ec} = \sqrt{B/\gamma}$. The surface tension γ was measured with the Krüss K6 manual tensiometer (deionized water showed a drop in surface tension when previously put in contact with a PAN membrane, from 72 mN/m to 53 mN/m). To test the dependence of the wavelength on surface tension, the experience was performed with deionized water and a water/soap solution (of measured surface tension $\gamma = 30$ mN/m). The membrane bending rigidity per unit depth B being low, it could not be measured experimentally. Therefore, it was roughly estimated as $B = \alpha\frac{t_0}{a}Ea^3$ where t_0 is the membrane dry thickness, a the typical radius of the fiber composing the membrane ($a = 250$ μm) and E is the PAN Young's modulus ($E \simeq 30$ GPa). Finally, α is a dimensionless parameter to account for the membrane porosity (here adjusted to the experiments using $\alpha = 2 \cdot 10^{-4}$).

Planar wicked membrane theory

We consider a rectangular fibrous membrane of initial length L and width W, attached to two parallel supports. The supports are initially separated by a distance $X = L$, see Figure S11. The membrane is wicked by a liquid and the distance X is decreased. During this compression, the membrane remains under tension due to the liquid surface tension and stores the excess membrane inside wrinkles and folds. These 'surface reservoirs' are afterwards recruited when the wicked membrane is put in extension. The reaction F from the supports is here analyzed, depending on X, W, L, and the surface tension γ.

We consider the potential energy of the wicked membrane and minimize it to find its equilibrium. As before we consider the surface energy of the liquid/air interface which is here identified with the surface of the membrane itself. The bending energy of the membrane is neglected and its extensional energy is replaced with a inextensibility constraint, thereby considering the extensional energy being much larger than the surface energy. The membrane can then easily wrinkle and fold but cannot be stretched, and surface tension tends to minimize the surface of the system. Only two of the membrane edges are attached to the supports, the other two edges remaining free, see Figure S11. In such a geometry, the free edges experience a normal force acting toward minimization of the surface of the system. Each edge therefore adopts the shape of a circular arc (*24*) and inextensibility impose their length to be L.

Early compression: $\frac{2}{\pi}L < X < L$

The distance X is decreased from $X = L$, and in this section we treat the case $\frac{2}{\pi}L < X < L$. As explained above we assume the free edges to describe circular arcs of length L and we introduce two variables R and β, respectively the radius and angle span of the circular arcs, see figure S11. R and β are related to L and X through two equations:

$$L = 2R\beta \tag{19}$$

$$X = 2R\sin\beta \tag{20}$$

The surface area of the liquid infused membrane then writes:

$$S = WX - 2(R^2\beta - RX\cos\beta) \tag{21}$$

where the term $R^2\beta$ corresponds to the surface area of an angular region (angle β) of a disc of radius R. The term $RX\cos\beta$ refers to the surface area of two right-angle triangles of hypotenuse R and side length $R\cos\beta$.

The reaction force F from the support is given by the derivative of the energy $2\gamma S$ with respect to X. We introduce the normalized force $f = F/2\gamma W$

$$f = \frac{1}{2\gamma W}\frac{\partial(2\gamma S)}{\partial X} \tag{22}$$

which we computed numerically.

Advanced compression: $0 < X < \frac{2}{\pi}L$

As X is decreased from $X = L$, β increases from $\beta = 0$. When X reaches $2L/\pi$, β reaches $\pi/2$ and for smaller values of X, the angle β no longer varies and the geometry of the system changes, see figure S12. The radius R of the circular arc remains of interest and a new variable Δ is considered, it represents the length on which the membrane adheres to the support. R and Δ are given by the 2 relations:

$$L = 2\Delta + \pi R \tag{23}$$

$$X = 2R \tag{24}$$

The surface of the wicked membrane is now given by

$$S = WX - 2X\Delta - \pi R^2 \tag{25}$$

Injecting the three previous relations in the force equation, Equation (22), we find an explicit expression for the force

$$f = 1 - \frac{L}{W}\left(1 - \frac{\pi x}{2}\right) \tag{26}$$

where $x = X/L$. The theoretical dimensionless force vs. displacement curves are given in figure S13 for four different values of the ratio L/W.

Cylindrical wicked membrane theory

Here, we consider a cylindrical geometry, reminiscent of the archetypal liquid soap catenoid. A dry membrane is folded into cylindrical shape with radius R_H and height $2L$. The membrane is then attached to two rigid parallel rings of radius R_H and then infused with a liquid. The potential energy of the system comprises bending, stretching, and surface energies, and as in the previous section the bending energy is neglected and the stretching energy is replaced by an inextensibility constraint. The surface energy of the liquid/air interface is $2\gamma S$ where γ is the liquid-vapor surface tension of the liquid, and S the surface area of the wicked membrane. As surface tension does not vary, the system seeks to minimize its surface area S given by

$$S(R(Y), R'(Y), H) = \int_{-H}^{H} 2\pi R\sqrt{1 + R(Y)'^2}\,\mathrm{d}Y \tag{27}$$

Moreover, as the fibers of the membrane are inextensible (they can wrinkle inside the liquid film, but cannot be stretched) we introduce a inequality constraint that imposes that the length of the curve $R = R(Y)$ is smaller than or equal to L:

$$g(R, R', H) = 2L - \int_{-H}^{H} \sqrt{1 + R'^2}\,\mathrm{d}Y \geq 0 \tag{28}$$

We therefore introduce a Kuhn-Tucker multiplier $2\pi\mu$ and work with the Lagrangian $\mathcal{L}$

$$S - 2\pi\mu\, g(R, R', H) = -4\pi\mu L + \int_{-H}^{H} 2\pi(R+\mu)\sqrt{1 + R'^2}\,\mathrm{d}Y = -4\pi\mu L + 2\pi \int_{-H}^{H} \mathcal{L}(R, R')\,\mathrm{d}Y \tag{29}$$

Kuhn-Tucker conditions for minimization imposes that $\mu \geq 0$, $g \geq 0$, $\mu\, g = 0$ and

$$\left(\frac{\partial \mathcal{L}}{\partial R'}\right)' = \frac{\partial \mathcal{L}}{\partial R} \quad \Rightarrow \quad R\,R'' = 1 - R'^2 \tag{30}$$

The solution of which is

$$R(Y) = c\,\cosh\left(\frac{Y - b}{c}\right) - \mu \tag{31}$$

where b and c are two integration constants. The symmetry condition $R'(0) = 0$ yields $b = 0$, and c is found with the boundary condition $R(H) = R_H$:

$$c\cosh\left(\frac{H}{c}\right) - \mu = R_H \tag{32}$$

Finally we deal with two cases: (i) the inequality constraint is active, $g = 0$, and μ is found with injecting (31) in (28):

$$c\sinh\left(\frac{H}{c}\right) = 2L \tag{33}$$

or (ii) the inequality constraint is inactive, $g > 0$, and $\mu = 0$. In any cases (32) and (33) are solved numerically.
Please note that when the inequality constraint is inactive, we are back with the usual liquid catenoid, only the surface area given in eq. (27) is in fact minimized.
We analyze the solutions by plotting the neck radii $R(Y = 0)$ as a function of the distance $2H$ between the two rings for different fixed rest lengths $2L$, see Figure S15. In this Figure, the usual liquid catenoid solution ($\mu = 0$) is plotted in blue and solutions with $g = 0$ are plotted in green. Along a green curve the part plotted with a continuous line is such that $\mu > 0$ and the part plotted with a dashed line is such that $\mu < 0$ (and are thus unstable). We see in Figure S15 that for some L values, a wicked membrane can display two stable catenoid shapes for the same height H. For example, the curve corresponding to $l = 1.4$ shows that for a given height h slightly below 1.0, the neck radius can be that of a pure liquid catenoid (blue curve), or that of a membrane catenoid (green curve). This bistability yields possible hysteresis behaviour for the system. Indeed, when the $l = 1.4$ membrane catenoid comes from $h > 1$ while decreasing h, it follows the green curve. As it crosses the unstable liquid catenoid solution (dotted blue line), μ changes sign and becomes negative, making the system unstable. The membrane catenoid then jumps to the stable liquid catenoid solution (solid blue curve). On its way back (increasing h) it follows the blue curve until it crosses $h = 1$ where the liquid catenoid looses stability. The system then jumps back on the membrane catenoid solution (green curve).

Orientation of the wrinkling pattern

In this Section, we experimentally observe the orientation of the wavy pattern patterns (i.e. the directions followed by the wrinkles all over the membrane) of a wicked membrane in three different configurations. In order to gain a deeper physical understanding of these patterns, we then turn to an analogous elastic plate problem under compression and solve it using a Finite Element Method. Determining the inner stress state of this plate for a similar geometry and under similar boundary conditions provides a glance into the wrinkling directionality of the wicked membrane.

Experimental observation

We focus on the wrinkling pattern displayed by a compressed planar wicked membrane and therefore study three cases. The first one corresponds to a wicked membrane in the absence of gravity. The second one is influenced by gravity and is set in a vertical position, its compression axis is perpendicular to the gravity field's direction. The third one corresponds to a rotated version (90°) of the previous one and has a compression axis parallel to gravity.

Absence of gravity

In the first case, since the visualization setup constrains a vertical position of the membrane, we turn to a thin PAN membrane (electrospun for 2 minutes) wicked with a little amount of water in order to limit the influence of gravity to a minimum. The precise quantity of wicking water is not defined in the experiment. However, by letting the infused water drain downwards for a few minutes, and then sponge it with a cloth, it is reduced to a small quantity. A typical visualization of this experiment is provided in Figure S16. The wrinkling pattern displays a satisfying top-down symmetry. The wrinkles show an angle at the top and bottom part of the membrane (see respective close-ups on these areas), and follow the direction of the circular arcs described by the top and bottom free edges. The wrinkles direction is vertical in the middle of the membrane.

Gravity perpendicular to compression axis

Now, a thicker membrane (electrospun for 4 minutes) is wicked with a larger amount of water and is again slightly compressed (about 5% compression). The observations are provided in Figure S17 where we see that gravity plays an important role in the wrinkling pattern as it now displays a top-down asymmetry. The wrinkles show an angle (they exhibit a 'V' shape) over the whole membrane except at the bottom where they describe a Λ shape. In both the bottom and top area, the wrinkle pattern adjusts to follow the circular arc described by the free edges.

Gravity parallel to global compression axis

The last experiment is performed on a thick membrane (electrospun for 4 minutes) wicked with a large amount of water. Unlike the previous experiment, the compression axis of the membrane is now parallel to the gravity field and the resulting wrinkling pattern again exhibits an obvious top-down asymmetry as presented in FIgure S18. Once again, the wrinkling pattern seems to adjust near the free edges to follow their circular shape.

Major compression axis criterion: Comparison with an elastic plate under compression

The orientation of the wavy pattern is likely dictated by the early stress state of the membrane just before wrinkling occurs. It is reasonable to assume that, being flexible, the membrane can not withstand compression and that it buckles instantaneously when compression occurs. When a wrinkle appears, it therefore likely takes the perpendicular direction to local compression axis in the membrane. In order to the approximate the stress state of the membrane at early compression, we turn to an elastic Finite Element Method (FEM) and compute the stress state of an analogous rectangular planar plate of width W and length L. As for the planar wicked membrane, the right and left edges of the plate are straight and brought closer by a length ΔL. In order to reproduce the geometry adopted the planar wicked membrane, a displacement is imposed at the top and bottom edges of the plate in order to reproduce circular arcs of fixed length L. The key ingredients of the numerical simulations are presented in the next sections.

Plate equations: plane stress condition

The deformation field $\boldsymbol{\varepsilon}$ of the plate is related to its displacement field $\boldsymbol{u}$ and is given by:

$$\boldsymbol{\varepsilon} = \frac{1}{2}\left(\boldsymbol{\nabla}\boldsymbol{u} + \boldsymbol{\nabla}^T\boldsymbol{u}\right) \tag{34}$$

or:

$$\varepsilon_{xx} = \frac{\partial u_x}{\partial x} \quad \text{and} \quad \varepsilon_{yy} = \frac{\partial u_y}{\partial y}; \quad \varepsilon_{xy} = \varepsilon_{yx} = \frac{1}{2}\left(\frac{\partial u_x}{\partial y} + \frac{\partial u_y}{\partial x}\right) \tag{35}$$

where no out of plane deformation is taken into account. Moreover, for a thin plate, the internal stress state shows no components on the z-axis (i.e. $\sigma_{zz} = \sigma_{xz} = \sigma_{yz} = 0$) and the stresses are therefore written (*25*):

$$\sigma_{xx} = \frac{E}{1-\nu^2}\left(\varepsilon_{xx} - \nu\varepsilon_{yy}\right); \quad \sigma_{yy} = \frac{E}{1-\nu^2}\left(\varepsilon_{yy} - \nu\varepsilon_{xx}\right) \quad \text{and} \quad \sigma_{xy} = \frac{E}{1+\nu}\,\varepsilon_{xy}. \tag{36}$$

The total elastic energy of the system writes:

$$\mathcal{V}_{\text{el}} = \iint \frac{1}{2} T\,\boldsymbol{\sigma} : \boldsymbol{\varepsilon}\,\mathrm{d}S \tag{37}$$

where T refers to the thickness of the plate. The gravitational energy of the system, is

$$\mathcal{V}_{\text{grav}} = -\iint \rho T\, \boldsymbol{g} \cdot \boldsymbol{u}\, \mathrm{d}S. \tag{38}$$

Boundary conditions

The straight edges (right and left) are brought closer in a linear way along the x-axis at a relative compression $\Delta L/L$.

$$\boldsymbol{u}_{\text{right}} = \big[-(L - \Delta L)/2,\, 0\big] \tag{39}$$

$$\boldsymbol{u}_{\text{left}} = \big[(L - \Delta L)/2,\, 0\big] \tag{40}$$

whereas the top and down free edges adopt circular shapes, while conserving their arc length L as described in Section 'Planar wicked membrane' (the variables R and β are found in that section).

$$\boldsymbol{u}_{\text{top}} = \left[R \sin\left(\frac{X_{\text{top}}}{R}\right) - X_{\text{top}},\, R\left(\cos\beta - \cos\left(\frac{X_{\text{top}}}{R}\right)\right)\right] \tag{41}$$

$$\boldsymbol{u}_{\text{bot}} = \left[R \sin\left(\frac{X_{\text{bot}}}{R}\right) - X_{\text{bot}},\, -R\left(\cos\beta - \cos\left(\frac{X_{\text{bot}}}{R}\right)\right)\right] \tag{42}$$

where X_{top} and X_{bot} respectively correspond to the X-coordinates of the nodes of the top and bottom free edges.

Numerical solution with FEniCS

FEniCS is an open-source computing platform for solving partial differential equations using a Finite Element Method (*26*) and we will here use it to numerically solve the problem exposed above by minimizing the total energy $\mathcal{V} = \mathcal{V}_{\text{el}} + \mathcal{V}_{\text{grav}}$ of the system. The calculations are performed for $L = 2$, $W = 6$, $\Delta L/L = 0.05$, $T = 0.001$, $E = 1$, $\rho g = 0$ (or 0.2 for the study of the influence of gravity, chosen arbitrarily) and the number of nodes meshing the plate is $N = 20 \times 20$.

Major compression criterion

Once the problem is solved numerically, we study the planar stress tensor $\boldsymbol{\sigma}$ at each node of the elastic plate. We compute its eigenvalues $\sigma_{1,2}$ and eigenvectors ($\boldsymbol{V}_{1,2}$) which reveal the principal stress directions throughout the plate. A positive eigenvalue σ_i ($i = 1, 2$) corresponds to tension state in the $\boldsymbol{V}_i$ direction whereas a negative one denotes compression. Therefore, finding the lowest eigenvalue σ_i and ensuring it is negative gives

access to the major compression axis, i.e the axis along which compression is the strongest. Transposed to the wicked membrane, this information is valuable. Indeed, since the membrane has a low bending rigidity, it cannot withstand any compression and it locally buckles inside the liquid film as soon as compression is present. If the membrane is subjected to two orthogonal compressions, it seems reasonable to assume that it will buckle first along the highest compression axis. The wrinkling lines would therefore appear perpendicularly to the major compression axis. A set of results for the three different cases discussed in the previous section is presented in Figure S19, where the elastic plate's stress field was computed using the parameters provided in Section . The lines correspond to the perpendicular directions of the eigenvector $\boldsymbol{V}_i$ ($i = 1, 2$) where σ_i is the lowest of the eigenvalues of $\boldsymbol{\sigma}$, and is negative.

Discussion

The numerical calculation of the orientation of the major compression axis in an elastic plate, presented in Figure S19, is in good qualitative agreement agreement with the experimental observations of Figures S16, S17 and S18. The stress state of the wicked membrane just before it starts wrinkling gives rise to the well defined wrinkling pattern; any local small compression will result in wrinkling of the membrane. Since the compressive stresses inside the membrane remain relatively low, a small exterior perturbation can significantly modify the wrinkling orientation. For example, Figure S20 shows a planar wicked PAN membrane in a slightly compressed state. Bubbles are present at its surface and the capillary forces they exert on the membrane are sufficient to locally distort the orientation of the wrinkling pattern. Indeed, the tension applied by the liquid meniscus seems to rotate the major compression axis of the membrane which therefore displays wrinkles perpendicular to the bubble periphery.

Polymer	**Solvent**	**Wicking liquid**
PAN	DMF	water - glycerol - ethanol - silicone oil
PVDF-HFP	DMF	ethanol - silicone oil
PCL	DMF	ethanol - silicone oil
PVP	ethanol	silicone oil

Table S1: Polymers used to fabricate fibrous membranes with their respective solvents and wicking liquids that are used to form surface reservoirs.

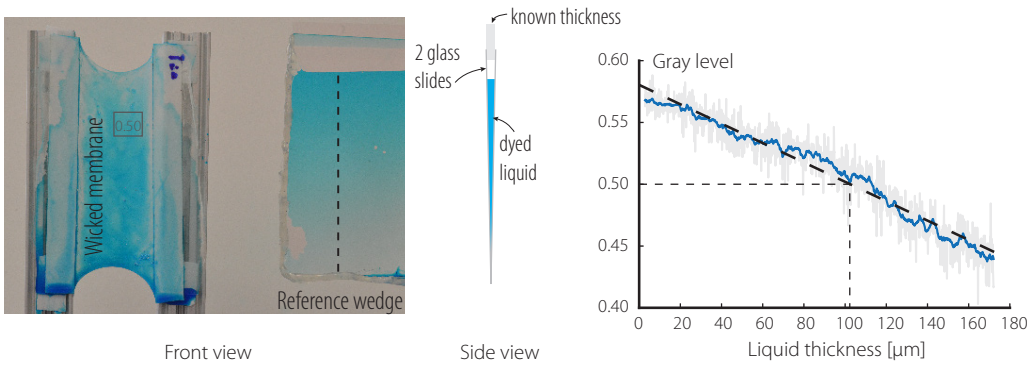

Figure S1: Measurement the liquid film thickness of the infused membrane with a colorimetry method. A scale wedge (two slightly non parallel glass slides) is used to calibrate the gray level as a function of colored liquid thickness on a photograph. In this case, we show an area on the membrane where the gray level is 0.50, corresponding to a liquid film thickness of around 100 μm.

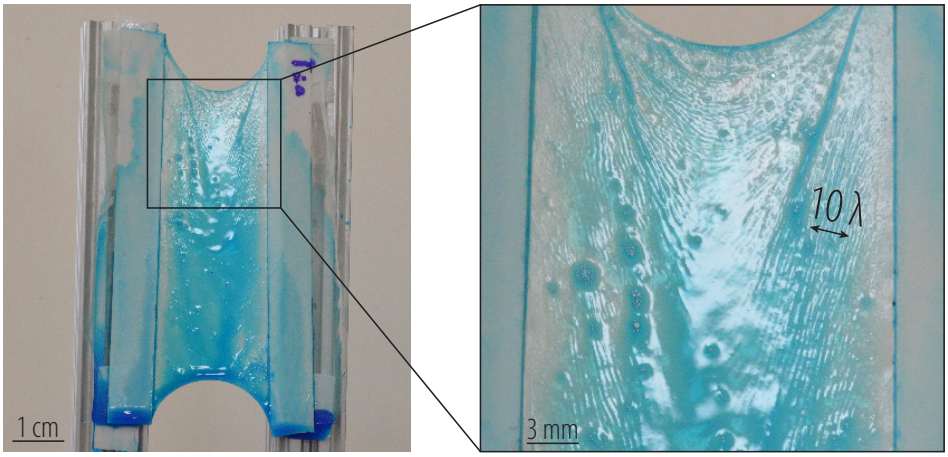

Figure S2: Visualization of the wrinkles on a slightly compressed membrane PAN membrane wicked with dyed water.

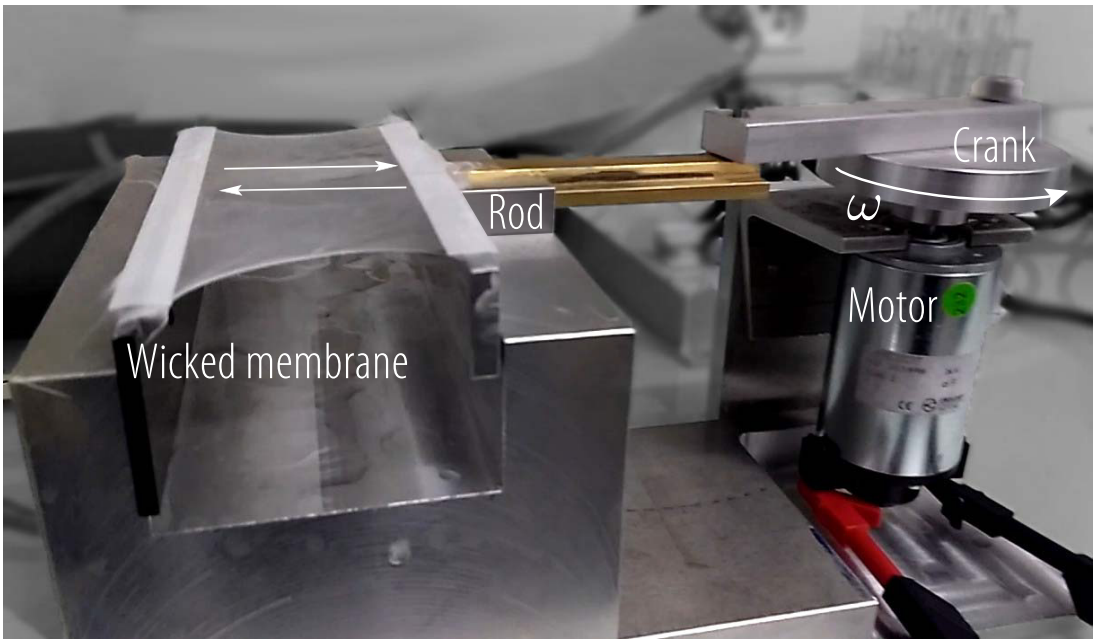

Figure S3: **Fatigue test setup.** In order to test their resistance to fatigue, the membranes are mounted on a motor-crank-rod setup, allowing to impose end displacement of one of the membrane edges from $X_{\min} = 2$ mm to $X_{\max} = 3.7$ cm (effective elongation of factor 18). The high cycling rate (here 3 cycles per second) allows to test a membrane in only a few days.

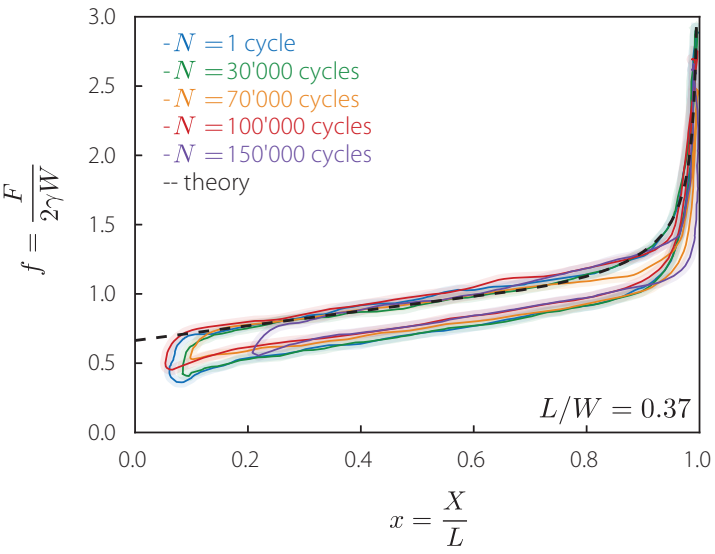

Figure S4: Force vs. displacement of the planar PVDF-HFP membrane during one compression-extension cycle after imposing N cycles to it. PVDF-HFP membrane wicked with v10 silicone oil ($\gamma = 21$ mN/m), $L/W = 0.37$.

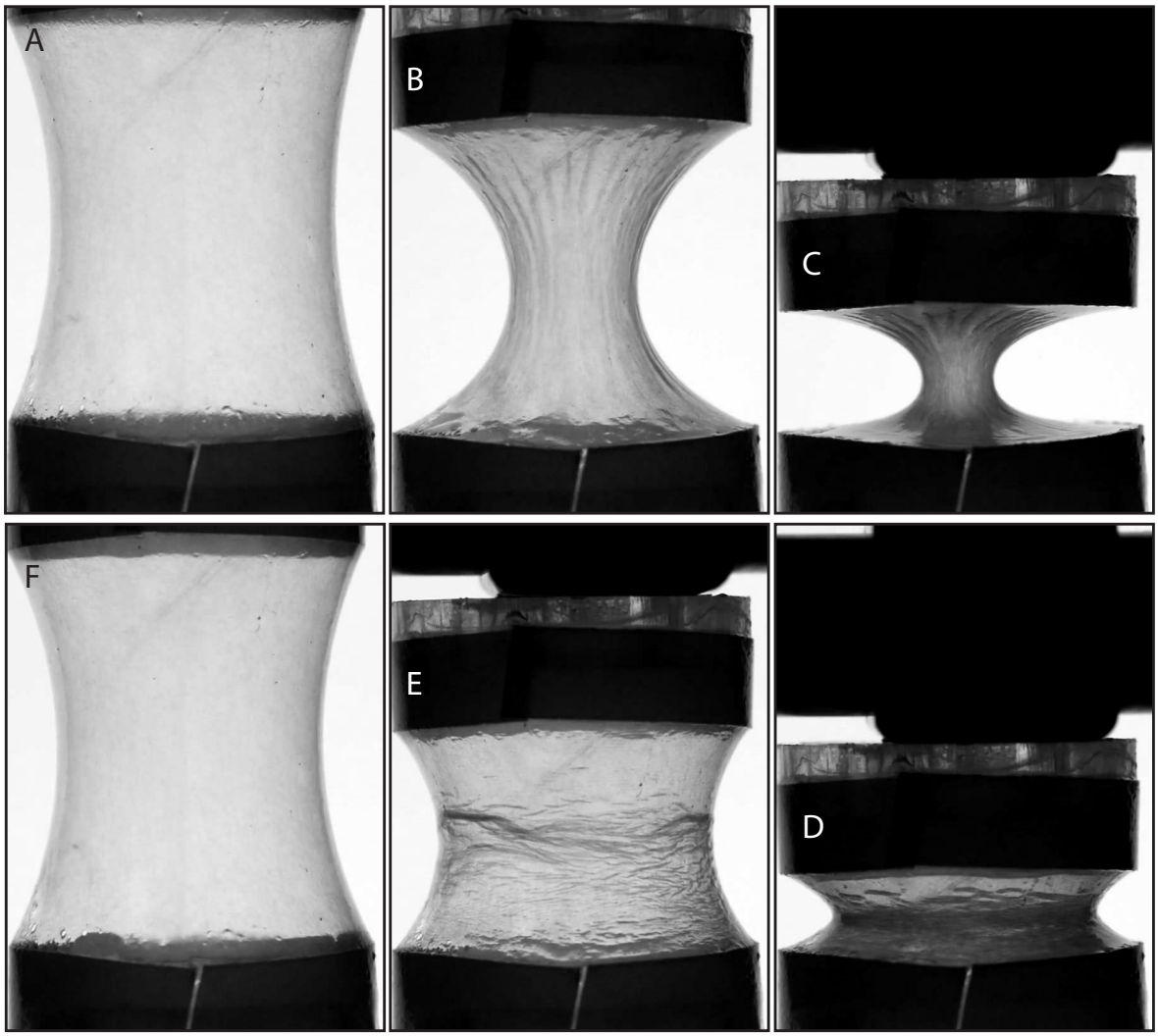

Figure S5: Cylindrical wicked membrane attached to two rings (diameter of the rings: $2R = 4$ cm) throughout a compression/extension cycle. Note that the this catenoid-shape jumps from a thin to wide state between image C and D. This sudden change in shape is due to an instability related to inextensibiliy of the membrane. Note the hysteresis of the system which does not follow the same paths during compression and extension.

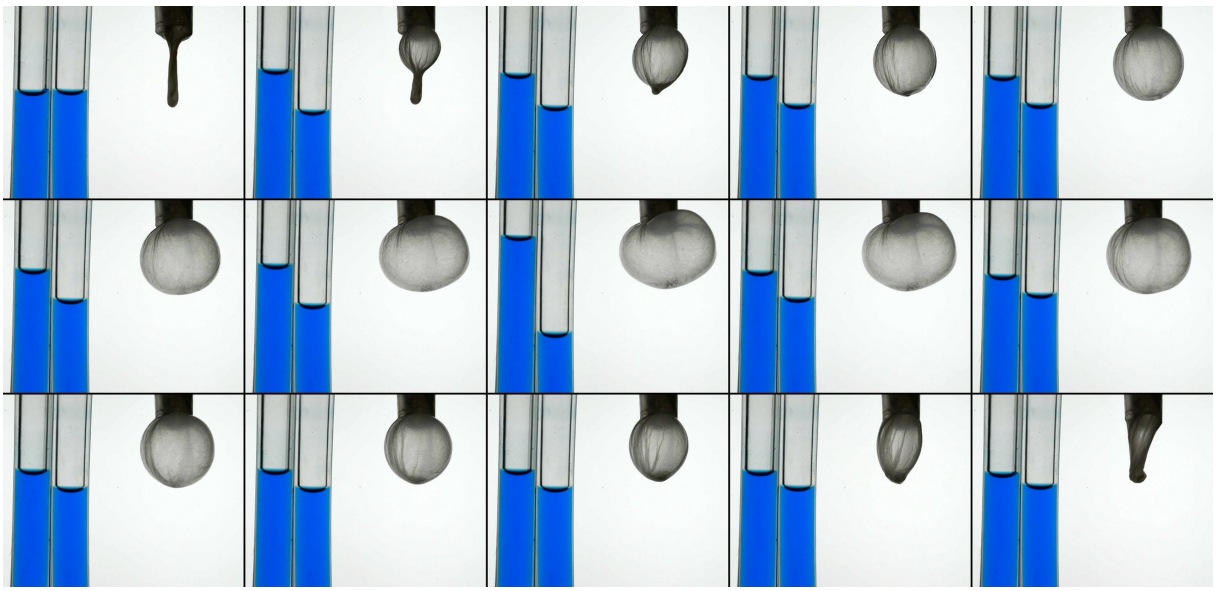

Figure S6: Bubble-like wicked membrane inflated with air. The tubes filled with blue dyed ethanol allow to characterize the pressure inside the wicked membrane bubble throughout its inflating. The external diameter of the bubble supporting tube is 9 mm.

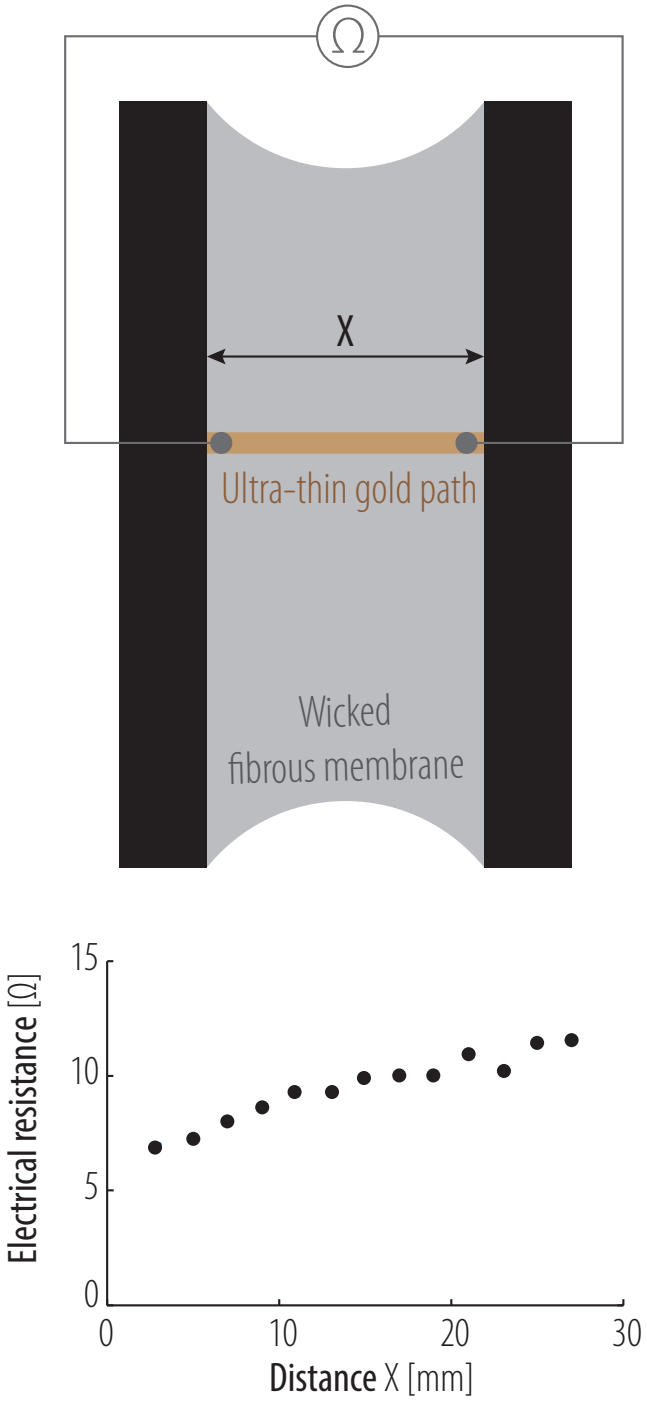

Figure S7: A thin gold path is affixed on a planar silicone oil-wicked PVDF-HFP membrane. When the straight edges of the wicked membrane are brought closer, the gold path is folded with the membrane reservoirs and conducts electricity throughout an 8-fold extension. End-to-end resistance of this conductive path depends on compression, likely due to self-contacts of the gold strip upon folding within the membrane reservoirs.

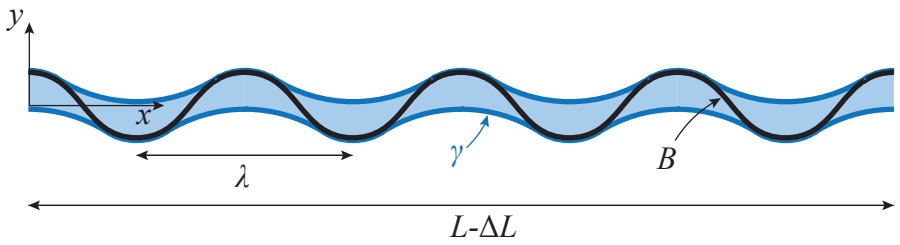

Figure S8: Wrinkling of a beam of length L under compression (ΔL) in a liquid film of volume per unit depth $V = hL$. The liquid/air interface (drawn blue) covers the beam near the max and min amplitude points along the beam. The beam has a bending resistance B and the buckling presents a periodicity of wavelength λ.

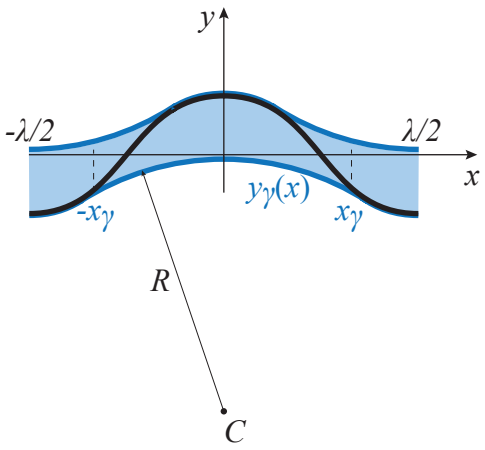

Figure S9: Local problem on one wavelength between $x = -\lambda/2$ and $\lambda/2$. The lower liquid interface (here blue), defined by $y_\gamma(x)$, describes and arc of circle (center C, radius R) between $-x_\gamma$ and x_γ. For $|x| > x_\gamma$, the liquid interface follows the beam profile.

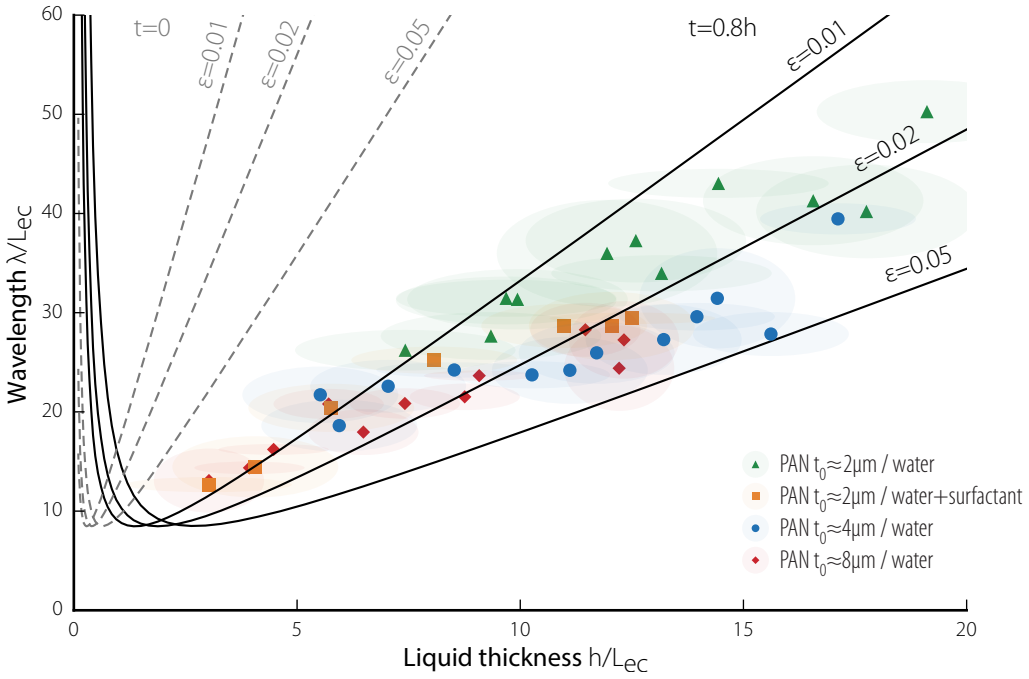

Figure S10: Dimensionless wavelength λ/L_{ec} versus dimensionless liquid thickness h/L_{ec}. The elasto-capillary length L_{ec} is defined as $\sqrt{B/\gamma}$ with B the bending stiffness per unit depth of the membrane and γ the surface tension of the wicking liquid. Note that the bending stiffness B per unit depth of the membrane depends on its native (dry) thickness t_0. The points show experimental results for different PAN-membrane dry ticknesses t_0 and different wicking liquids. The gray solid lines are results of the here presented model for $\Delta = \epsilon = 0.01,\ 0.02,\ 0.05$. It is considered that the membrane grows as it is infused with liquid. To capture this growth, we choose the membrane thickness t to be proportional to the liquid thickness h, with $t = 0.8h$. The gray dotted lines represent the same results for a zero-thickness beam.

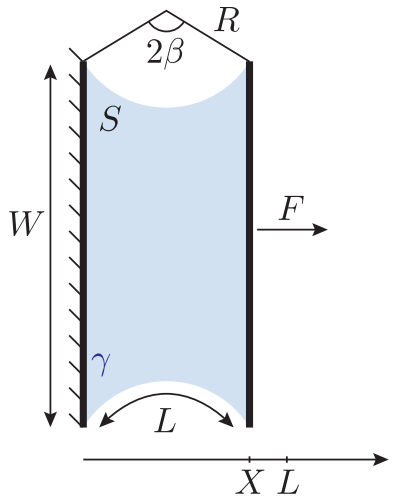

Figure S11: Planar wicked membrane during early compression. The surface minimization with isoperimetric constraint on the free edges of the wicked membrane is responsible for the circular shape adopted by these free edges.

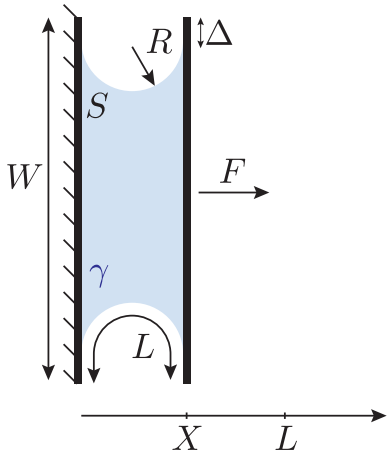

Figure S12: Schematic representation of a planar wicked membrane in a large compression state.

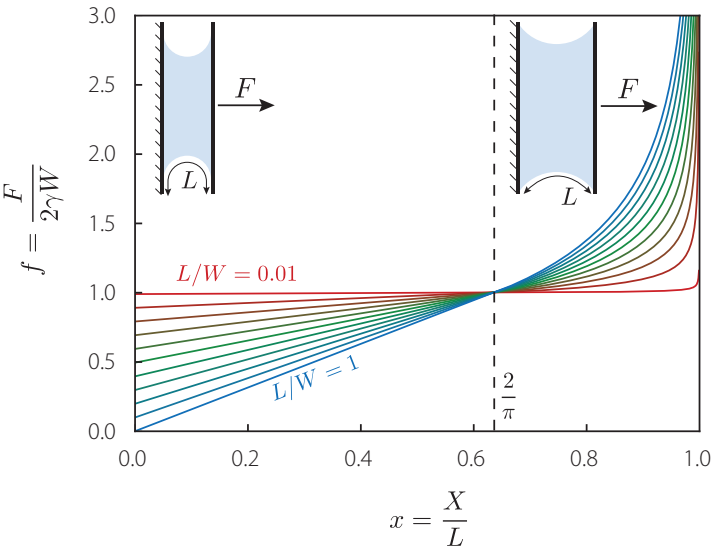

Figure S13: Theoretical normalized force versus displacement curve of the planar wicked membrane for different initial length to width ratios L/W ranging from 0.01 to 1. Note that when L/W approaches 0 (i.e. the length of the free edges is very small compared to the width of the membrane), the force vs. displacement curve approaches that of liquid film on a frame ($f = 1$) up until $x = 1$ where the inextensibilty of the membrane makes the force diverge.

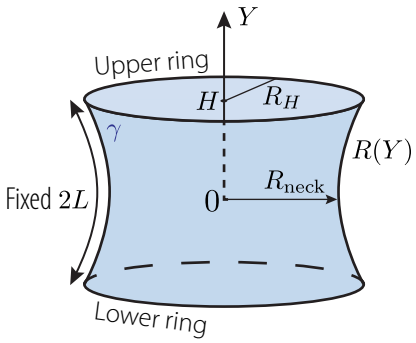

Figure S14: Schematic representation of the catenoid-like shape adopted by a cylindrical wicked membrane attached to two parallel rings.

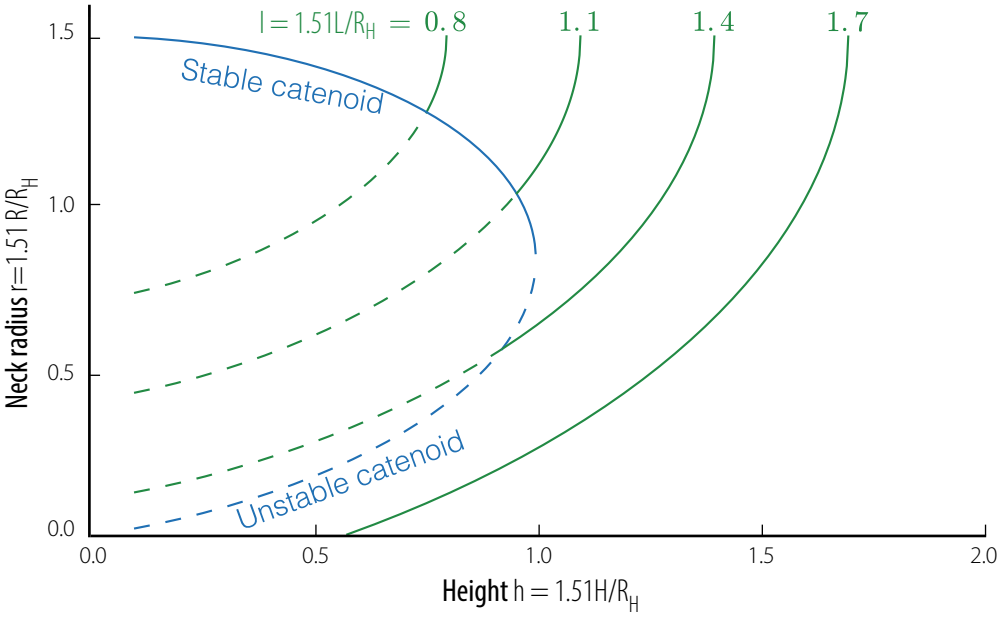

Figure S15: **Dimensionless neck radius r versus dimensionless distance between the two rings** h for different length constraints l. The length $R_h/1.5090$ is commonly used to normalize lengths in catenoid-related problems. Note that inextensibibilty of the membrane allows for equilibrium solutions to exist in the region $h > 1$, where purely liquid catenoids do not exist. Solid green lines represent solutions where the inequality constraint (28) is active, $g = 0$, and $\mu > 0$. The are drawn for different values of the membrane initial height $2L$. Dotted green lines represent solutions with $g = 0$ but $\mu < 0$ and are thus unstable. The solid and dotted blue line respectively represent the stable and unstable purely liquid catenoid, with $\mu = 0$.

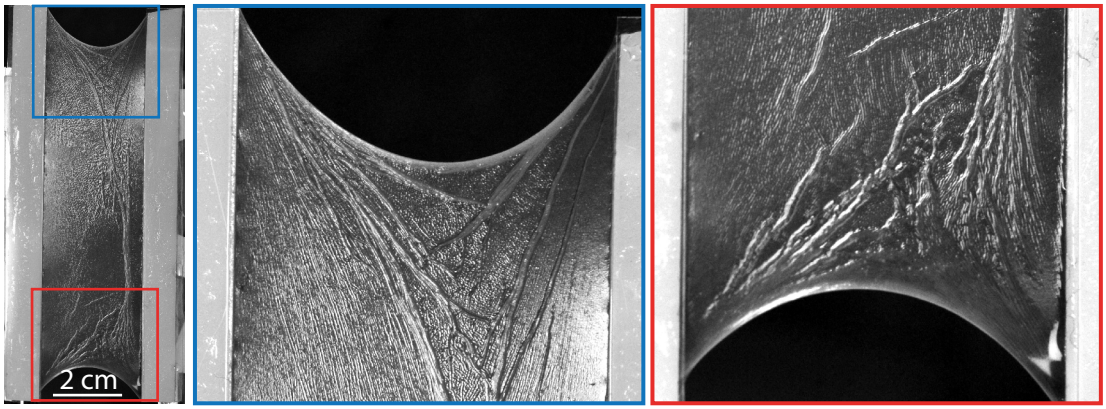

Figure S16: Thin PAN membrane wicked with a small quantity of water. The resulting wrinkling pattern follows a well defined structure and has a satisfying top-down symmetry. A previous compression may have concentrated the liquid at the right side, therefore generating the left-right asymmetry that is observed.

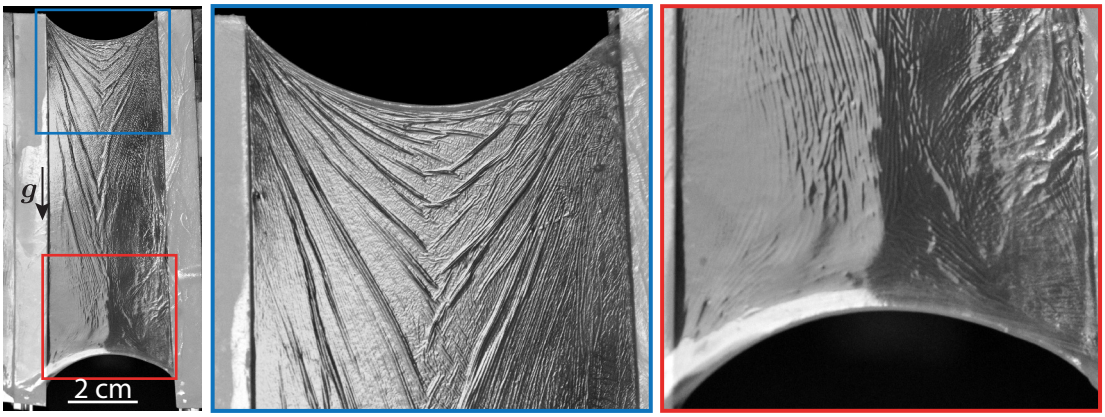

Figure S17: Thick PAN membrane wicked with a large amount of water. Here, gravity plays an important role in the pattern adopted by the wrinkles. It displays a 'V' structure on the whole membrane, except at the bottom of it, where the 'V' is inverted and the wrinkles direction follow the circular arc described by the free edge.

Figure S18: Thick PAN membrane wicked with a large amount of water. Unlike the case presented in Figure S17, gravity now is oriented in the same direction as the compression axis of the membrane. This results in a wrinkling pattern where again, the preferred directions follow the circular arcs of the free edges. It should be noted that the inhomogeneities in the membrane's color density correspond differences in thickness, but they do not affect the wrinkling pattern significantly.

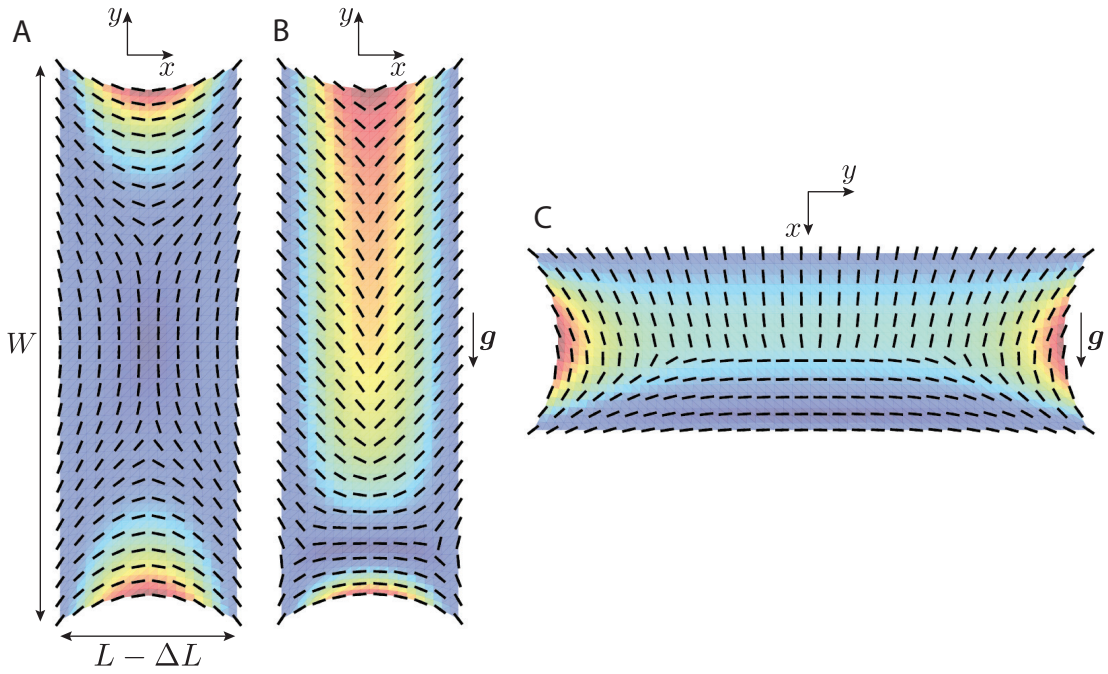

Figure S19: **An elastic planar plate under compression to read the major local compression axes.** Calculations performed with FEniCS. There is no gravity in **A** while **B** and **C** respectively correspond to calculations with gravity pointing perpendicular and parallel to the plate's global compression axis. The straight black lines show the orthogonal directions to the local major compression axes and thus show the direction along which wrinkles are generated in the wicked membrane case. Qualitatively, we find a good match between the patterns predicted by the elastic planar plate model and the experimental wicked membrane wrinkling patterns (resp. presented in Figures S16, S17 and S18). All the calculations are performed with $L = 2$, $W = 6$, $T = 0.001$, $E = 1$, $\nu = 0$, $N = 20 \times 20$, $\Delta L/L = 0.05$ and $\rho g = 0.2$ (ρg was arbitrarily chosen) for **B** and **C**. The color scale refers to the displacement field.

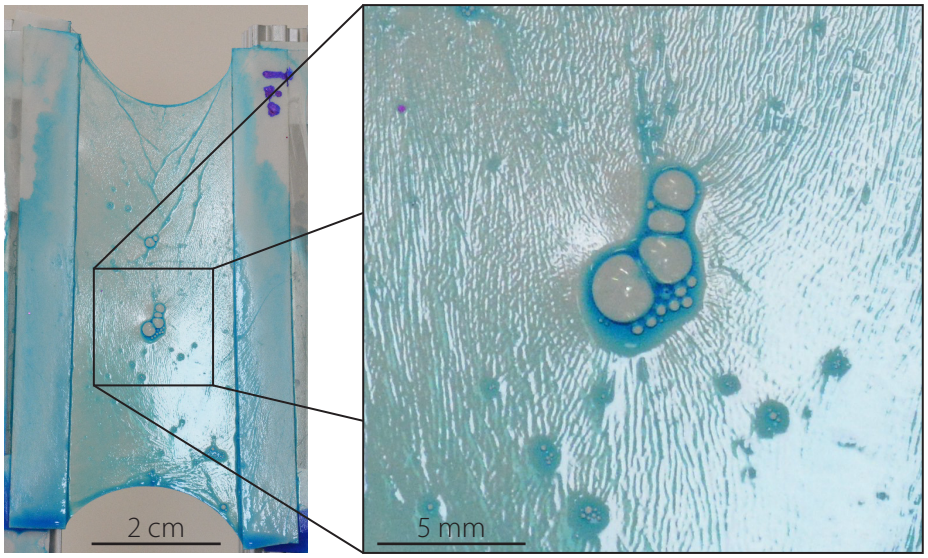

Figure S20: PAN membrane wicked with a water-surfactant solution. A bubble is present at the surface and the capillary forces it applies are sufficient to significantly distort the wrinkling orientation which locally points perpendicularly to the bubbles' periphery.

Captions for Movies S1 to S10

Movie S1: Ultra stretchable wicked membrane
Successive photographs. Diameter of the membrane at its extended state: 7 cm. A PVDF-HFP fibrous membrane is attached to eight translational supports. When wicked with silicone oil, it immediately tightens up, even when compressed. Excess membrane is stored in surface-reservoirs through the formation of wrinkles and folds within the liquid film.

Movie S2: Wrinkling and packing of the wicked membrane
Real time. Width of the image: 1.3 cm. Planar PAN fibrous membrane wicked with deionized water. When the two straight edges of the membrane are brought closer, the wicked membrane exhibits a first wavy pattern and rapidly displays a second stacked accordion-like phase where the membrane is closely packed inside the liquid film.

Movie S3: Planar wicked membrane
Real time. Width of the membrane at its extended state: 3.7 cm. PVDF-HFP fibrous membrane wicked with silicone v100 oil. When the straight supports are brought closer, the membrane remains globally flat and taut; excess membrane is stored in membrane reservoirs, generated in the form of wrinkles and folds within the liquid film.

Movie S4: Catenoid equilibrium shape of a wicked membrane
Real time. Diameter of the upper and lower rings: 4 cm. PAN fibrous membrane wicked with deionized water in a cylindrical configuration. As the two supporting rings are brought closer, the shape adopted by the cylindrical wicked membrane tends to minimize global surface area. Between the 20^{th} and the 27^{th} second of the movie, the neck of this catenoid-like shape widens up significantly. This strong shape change is due to the asymmetry of the inextensibility constraint of the membrane. At first, when the rings are far away, the minimum-energy state of the wicked membrane sets its fibers in tension in the axial direction due to the inextensibility constraint. When the rings are brought closer, near the 20^{th} second of the movie, the minimum-energy state now leads to a shortening of the side length of the membrane. As the membrane can shrink by folding within the liquid film, a new, wider, configuration is selected. The morphology of the cylindrical wicked membrane is studied in detail in the Supplementary Material: Cylindrical wicked membrane theory.

Movie S5: Inflating a wicked membrane bubble
Real time. Diameter of the tube supporting the bubble: 9 mm. PAN fibrous membrane wicked with deionized water. The blue dyed ethanol semi-filled tubes allow for pressure measurement of the bubble throughout its inflating.

Movie S6: Zircon bead dipped in dyed deionized water
Real time. Diameter of the bead: 1.5 cm. A zircon bead is dipped in a dyed deionized-water bath and subsequently pulled out. Water partially wets zircon and the experiment leads to drops sitting at the bead surface.

Movie S7: Hydrophilic PAN membrane applied on a zircon bead dipped in dyed deionized water
Real time. Diameter of the bead: 1.5 cm. A zircon bead is covered with a thin dry fibrous PAN membrane (electrospun for 2 minutes) and dipped in a dyed deionized-water bath and subsequently pulled out. Since PAN is hydrophilic, capillarity makes the membrane fold and adapt to the bead shape within the liquid film. After dipping the PAN-membrane-covered bead around 10 times, it is pulled out with a fairly homogeneous dyed-water coating; although the membrane is folded inside the liquid film, the latter displays a smooth interface with air.

Movie S8: Silicon-oil wicked PVDF-HFP membrane applied a zircon bead dipped in dyed deionized water
Real time. Diameter of the bead: 1.5 cm. A zircon bead is covered with a thin fibrous PVDF-HFP membrane (electrospun for 2 minutes) and wicked with v3 silicone oil. The bead is then dipped in a dyed deionized water bath and subsequently pulled out. The silicone-oil wicked PVDF-HFP membrane acts as a water repellent coating as no water is drawn by the bead as it is pulled out of the bath.

Movie S9: Silicone oil-wicked PVDF-HFP membrane applied on a spherical glass surface provides a water reppellent treatment.
Slowed 125 times. Width of the image: 5 cm. A fibrous PVDF-HFP membrane is applied on a spherical glass substrate and wicked with silicone oil. The wicked membrane adapts to the curvature of the glass substrate by folding membrane within the liquid silicone-oil film. The resulting membrane reservoirs allow the storing of folds within the liquid film, thus keeping a relatively smooth transparent surface with water-repellent properties.

Movie S10: Stretchable electronics with the wicked membrane
Successive photographs. Width of the membrane at its extended state: 3.8 cm. A PVDF-HFP fibrous membrane is wicked by silicone oil and two thin gold strips are attached to it through capillary adhesion, and connected to a 1.5V LED. When voltage is supplied, the LED remains illuminated even during a compression/extension cycle (effective extension from compressed state: 800%).

Description of Experimental Data files

Data S1: Experimental wrinkling wavelength
Experimental wrinkling wavelength λ for a slightly compressed wicked PAN-membrane for different dry-membrane thicknesses t_0, wicking liquid surface tension γ and liquid thickness h. These results are presented in figure 2D and figure S10.

Data S2: Planar configuration force vs. displacement at the 1st cycle
Experimental data: normalized force vs. normalized displacement in the planar configuration at the first loading cycle. These results are presented in figure 3C and figure S4.

Data S3: Planar configuration force vs. displacement after 30,000 cycles
Experimental data: normalized force vs. normalized displacement in the planar configuration after 30,000 loading cycles. These results are presented in figure S4.

Data S4: Planar configuration force vs. displacement after 70,000 cycles
Experimental data: normalized force vs. normalized displacement in the planar configuration after 70,000 loading cylcls. These results are presented in figure S4.

Data S5: Planar configuration force vs. displacement after 100,000 cycles
Experimental data: normalized force vs. normalized displacement in the planar configuration after 100,000 loading cycles. These results are presented figure 3C and in figure S4.

Data S6: Planar configuration force vs. displacement after 150,000 cycles
Experimental data: normalized force vs. normalized displacement in the planar configuration after 150,000 loading cycles. These results are presented in figure S4.

Data S7: Cylindrical configuration neck radius vs. ring distance
Experimental data corresponding to the cylindrical configuration presented in figure 3F. r and h respectively correspond to the normalized neck radius and normalized distance between the supporting rings.

Data S8: Spherical configuration radius vs. pressure
Experimental data corresponding to the spherical configuration presented in figure 3I. r and p respectively correspond to the normalized bubble radius and the normalized pressure inside the bubble.

Data S9: Electrical resistance vs. end-to-end distance
Experimental data corresponding to the electrical resistance vs. end-to-end distance for a gold path on a silicone-oil wicked PVDF-HFP membrane. The results are presented in figure S7.

References

1. H. Elettro, S. Neukirch, F. Vollrath, A. Antkowiak, In-drop capillary spooling of spider capture thread inspires hybrid fibers with mixed solid-liquid mechanical properties. *Proc. Natl. Acad. Sci. U.S.A.* **113**, 6143–6147 (2016). doi:10.1073/pnas.1602451113 Medline

2. J. Lam, M. Herant, M. Dembo, V. Heinrich, Baseline mechanical characterization of J774 macrophages. *Biophys. J.* **96**, 248–254 (2009). doi:10.1529/biophysj.108.139154 Medline

3. L. Guillou, A. Babataheri, M. Saitakis, A. Bohineust, S. Dogniaux, C. Hivroz, A. I. Barakat, J. Husson, T-lymphocyte passive deformation is controlled by unfolding of membrane surface reservoirs. *Mol. Biol. Cell* **27**, 3574–3582 (2016). doi:10.1091/mbc.E16-06-0414 Medline

4. D. Raucher, M. P. Sheetz, Characteristics of a membrane reservoir buffering membrane tension. *Biophys. J.* **77**, 1992–2002 (1999). doi:10.1016/S0006-3495(99)77040-2 Medline

5. J. Dai, M. P. Sheetz, Mechanical properties of neuronal growth cone membranes studied by tether formation with laser optical tweezers. *Biophys. J.* **68**, 988–996 (1995). doi:10.1016/S0006-3495(95)80274-2 Medline

6. N. Groulx, F. Boudreault, S. N. Orlov, R. Grygorczyk, Membrane reserves and hypotonic cell swelling. *J. Membr. Biol.* **214**, 43–56 (2006). doi:10.1007/s00232-006-0080-8 Medline

7. J. A. Nichol, O. F. Hutter, Tensile strength and dilatational elasticity of giant sarcolemmal vesicles shed from rabbit muscle. *J. Physiol.* **493**, 187–198 (1996). doi:10.1113/jphysiol.1996.sp021374 Medline

8. C. A. Erickson, J. P. Trinkaus, Microvilli and blebs as sources of reserve surface membrane during cell spreading. *Exp. Cell Res.* **99**, 375–384 (1976). doi:10.1016/0014-4827(76)90595-4 Medline

9. S. Majstoravich, J. Zhang, S. Nicholson-Dykstra, S. Linder, W. Friedrich, K. A. Siminovitch, H. N. Higgs, Lymphocyte microvilli are dynamic, actin-dependent structures that do not require Wiskott-Aldrich syndrome protein (WASp) for their morphology. *Blood* **104**, 1396–1403 (2004). doi:10.1182/blood-2004-02-0437 Medline

10. G. Salbreux, G. Charras, E. Paluch, Actin cortex mechanics and cellular morphogenesis. *Trends Cell Biol.* **22**, 536–545 (2012). doi:10.1016/j.tcb.2012.07.001 Medline

11. J. A. Rogers, T. Someya, Y. Huang, Materials and mechanics for stretchable electronics. *Science* **327**, 1603–1607 (2010). doi:10.1126/science.1182383 Medline

12. W. Liu, M.-S. Song, B. Kong, Y. Cui, Flexible and stretchable energy storage: Recent advances and future perspectives. *Adv. Mater.* **29**, 1603436 (2017). doi:10.1002/adma.201603436 Medline

13. J. Hu, H. Meng, G. Li, S. I. Ibekwe, A review of stimuli-responsive polymers for smart textile applications. *Smart Mater. Struct.* **21**, 053001 (2012). doi:10.1088/0964-1726/21/5/053001

14. R. F. Shepherd, F. Ilievski, W. Choi, S. A. Morin, A. A. Stokes, A. D. Mazzeo, X. Chen, M. Wang, G. M. Whitesides, Multigait soft robot. *Proc. Natl. Acad. Sci. U.S.A.* **108**, 20400–20403 (2011). doi:10.1073/pnas.1116564108 Medline

15. A. Lazarus, P. M. Reis, Soft actuation of structured cylinders through auxetic behavior. *Adv. Eng. Mater.* **17**, 815–820 (2015). doi:10.1002/adem.201400433

16. See supplementary materials.

17. E. Cerda, L. Mahadevan, Geometry and physics of wrinkling. *Phys. Rev. Lett.* **90**, 074302 (2003). Medline

18. T. Tallinen, J. Y. Chung, F. Rousseau, N. Girard, J. Lefevre, L. Mahadevan, On the growth and form of cortical convolutions. *Nat. Phys.* **12**, 588–593 (2016). doi:10.1038/nphys3632

19. H. Vandeparre, M. Piñeirua, F. Brau, B. Roman, J. Bico, C. Gay, W. Bao, C. N. Lau, P. M. Reis, P. Damman, Wrinkling hierarchy in constrained thin sheets from suspended graphene to curtains. *Phys. Rev. Lett.* **106**, 224301 (2011). Medline

20. B. Davidovitch, R. D. Schroll, D. Vella, M. Adda-Bedia, E. A. Cerda, Prototypical model for tensional wrinkling in thin sheets. *Proc. Natl. Acad. Sci. U.S.A.* **108**, 18227–18232 (2011). doi:10.1073/pnas.1108553108 Medline

21. B. Roman, J. Bico, Elasto-capillarity: Deforming an elastic structure with a liquid droplet. *J. Phys. Condens. Matter* **22**, 493101 (2010). doi:10.1088/0953-8984/22/49/493101 Medline

22. B. Roman, A. Pocheau, Buckling cascade of thin plates: Forms, constraints and similarity. *Europhys. Lett.* **46**, 602–608 (1999). doi:10.1209/epl/i1999-00306-3

23. B. Audoly, Y. Pomeau, *Elasticity and Geometry: From Hair Curls to the Nonlinear Response of Shells* (Oxford Univ. Press, 2010).

24. P. Bérest, *Calcul des variations: Application a la mécanique et à la physique* (Ellipses, 1998).

25. Z. P. Bazant, L. Cedolin, *Stability of Structures: Elastic, Inelastic, Fracture, and Damage Theories* (World Science, 2010).

26. A. Logg, K.-A. Mardal, G. Wells, *Automated Solution of Differential Equations by the Finite Element Method: The FEniCS Book* (Springer, 2012).